Metastable condensates suppress conversion to amyloid fibrils

Tapojyoti Das[1]†, Fatima Zaidi[1]†, Mina Farag[2], Kiersten M. Ruff[2], James Messing[3], J. Paul Taylor[3], Rohit V. Pappu[2]*, Tanja Mittag[1]*

[1]Department of Structural Biology, St. Jude Children's Research Hospital; Memphis, TN 38105, USA.

[2]Department of Biomedical Engineering and Center for Biomolecular Condensates, Washington University in St. Louis; St. Louis, MO 63130, USA.

[3]Department of Cell and Molecular Biology, St. Jude Children's Research Hospital; Memphis, TN 38105, USA.

† These authors contributed equally to this work.

*Corresponding authors. Email: pappu@wustl.edu; tanja.mittag@stjude.org

Abstract: Stress granules form via co-condensation of RNA binding proteins with prion-like low complexity domains (PLCDs) and RNA molecules released by stress-induced polysomal runoff. Homotypic interactions among PLCDs can drive amyloid fibril formation and this is enhanced by ALS-associated mutations. We find that homotypic interactions that drive condensation versus fibril formation are separable for A1-LCD, the PLCD of hnRNPA1. These separable interactions lead to condensates that are metastable versus fibrils that are globally stable. Metastable condensates suppress fibril formation, and ALS-associated mutations enhance fibril formation by weakening condensate metastability. Mutations designed to enhance A1-LCD condensate metastability restore wild-type behaviors of stress granules in cells even when ALS-associated mutations are present. This suggests that fibril formation can be suppressed by enhancing condensate metastability through condensate-driving interactions.

One-Sentence Summary: In PLCDs, fibril formation driven by zipper motifs is suppressed by condensation-driving interactions mediated by stickers.

Introduction

Cytoplasmic stress granules (SGs) form in response to polysomal runoff caused by cellular stresses, and they disassemble once stresses abate. SGs are inhomogeneous biomolecular condensates that form via condensation, that combines reversible binding, oligomerization, phase separation, and percolation via a blend of homotypic and heterotypic interactions (*1-3*). SG assembly is driven by a core protein-RNA interaction network involving mRNA, the RNA-binding proteins (RBPs) G3BP1/2, TIA1, CAPRIN1 and other RBPs including FUS, TDP-43, hnRNPA1, and hnRNPA2 (*1-4*). The pathogenesis of neurodegenerative and neuromuscular disorders such as amyotrophic lateral sclerosis (ALS), frontotemporal dementia, inclusion body myopathy, and related diseases that are collectively known as multisystem proteinopathy (MSP) are associated with aberrant SG assembly and arrested disassembly (*5*). Cytoplasmic inclusions comprising insoluble deposits of SG proteins are among the defining pathological hallmarks of MSP (*6-9*).

Many mutations that lead to familial forms of MSPs occur within intrinsically disordered, prion-like low-complexity domains (PLCDs) of RBPs, and these mutations promote the dynamical arrest of SGs and enhance the formation of amyloid fibrils (*10-13*). This has led to the proposal that SGs serve as crucibles of amyloid formation whereby the high local concentration of PLCDs

enables fibril-driving homotypic interactions among so-called zipper motifs (*14*). However, other evidence suggests that localization of TDP-43 to SGs may be protective and that the localization of TDP-43 to other types of condensates with a lower capacity to prevent TDP-43 fibrillization may be a key step in disease pathogenesis (*15*). At this juncture, it is unclear if condensates are crucibles for fibril formation or if they are off-pathway sinks. We address this issue through direct measurements and find that condensates act as sinks for soluble proteins that suppress fibril formation.

Results

We characterized the interplay between condensation and fibril formation for A1-LCD, which is the PLCD from hnRNPA1 (**Fig. 1A**). The mutations D262N and D262V cause familial forms of MSP (*10*). *In vitro*, the A1-LCD variants (**Fig. S1A**) were exchanged from a denaturing to a native buffer without excess salt. Addition of NaCl to a final concentration of 150 mM induces condensation (**Fig. 1B**). Fibrils visible by light microscopy are evident after several hours, and the pathogenic mutations D262V and D262N enhance the rates of fibril formation when compared to the WT A1-LCD in concentration regimes where condensates can form (**Fig. 1B**) (*10, 16*).

Condensates and fibrils are, respectively disordered and ordered phases formed by the same proteins (*17-20*). The formation of each phase will be defined by a distinct saturation concentration (*17-21*). We denote the saturation concentrations for fibril formation and condensation as c_{sf} and c_{sc}, respectively. If $c_{sf} < c_{sc}$, then condensates are metastable phases when compared to fibrils. What is needed are direct measurements of c_{sf} versus c_{sc}.

A1-LCD condensates are metastable with respect to fibrils and pathogenic mutations reduce the metastability.

We measured c_{sc} and c_{sf} for different A1-LCD variants. To induce condensation, the A1-LCD variants were exchanged from a denaturing to a native buffer without excess salt. Addition of NaCl to a final concentration of 150 mM induces condensation as evidenced by the formation of fluid-like condensates that undergo fusion and demonstrate wetting behaviors. These behaviors are similar for WT A1-LCD and pathogenic mutants (**Fig. 1C**). We separated the dilute from the dense phase using sedimentation (*22, 23*) and measured the concentration of protein remaining in the dilute phase to quantify c_{sc} for each variant. A1-LCDs with pathogenic mutations have slightly higher c_{sc} values, pointing to a weakening of the driving forces for condensation (**Fig. 1D** and **Fig. S1B**). Given the small differences in c_{sc} values, we designed additional variants in which we mutated all four aspartate residues to either valine or asparagine (−4D+4V and −4D+4N, respectively). The c_{sc} values for the designed variants increase substantially vis-à-vis WT A1-LCD (**Fig. 1D**, **Fig. S1B**). This can be explained by the fact that removal of aspartate residues is accompanied by increased net charge per residue (NCPR) (*23*) (see **Fig. S1C**). Residues in PLCDs have been classified as stickers or spacers based on computed and measured hierarchies of interactions mediated by different residues (*22-24*). In the context of condensate formation, stickers form reversible physical crosslinks with one another, and spacers determine the solvation preferences of molecules and the cooperativity between percolation, a networking transition, and phase separation, a density transition (*23-25*). To probe the effects of valine independently of the effect of increasing the NCPR, we replaced three glycine residues and one serine with valine to generate the variant −3G1S+4V. This variant had a higher c_{sc} value relative to the WT A1-LCD, demonstrating that valine residues function as solvation-enhancing spacers in the context of the A1-LCD (**Fig. 1D, Fig. S1B**).

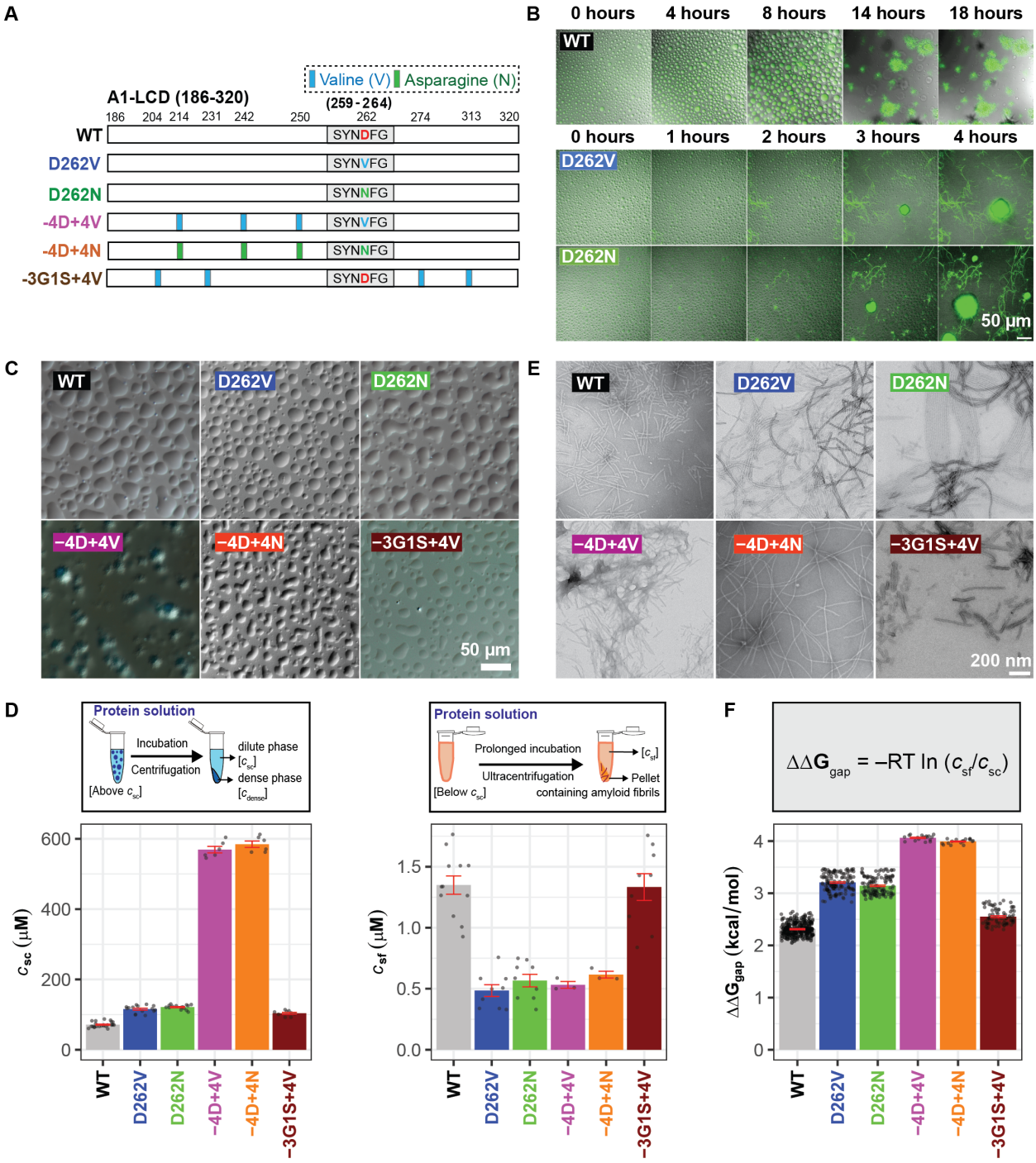

Figure 1: Pathogenic mutations reduce the metastability of A1-LCD condensates.
(A) Schematic of the sequence architectures showing a zipper motif within A1-LCD WT, pathogenic mutants, and designed variants that encompass the pathogenic mutations (−4D+4V and −4D+4N) or the WT sequence (−3G1S+4V). Vertical bars indicate the position of substitutions to valine (light blue) or asparagine (green). The zipper motif that is known to mediate fibril formation (S_{259}YNDFG_{264}) is denoted as a grey rectangle. **(B)** Time course of superimposed differential interference contrast (DIC) and thioflavin T (ThT) fluorescence microscopy images of solutions of A1-LCD variants showing condensates and the appearance of fibrils. **(C)** DIC micrographs of condensates of A1-LCD variants at similar degrees of supersaturation S_c (WT (120 µM, S_c = 0.52, D262V (200 µM, S_c = 0.55), D262N (200 µM, S_c = 0.50), –4D+4V (950 µM, S_c = 0.51), –4D+4N (950 µM, S_c = 0.48), –3G1S+4V (180 µM, S_c = 0.54)) with respect

to the phase boundary (sequence-specific value of c_{sc}) for condensate formation. **(D)** (Top left) Schematic depicting the sedimentation method [30] used to measure c_{sc}, and (bottom left) plot of c_{sc} of A1-LCD variants at 20 °C, and (top right) schematic depicting the method used to obtain the threshold concentration for fibril formation (c_{sf}) and (bottom right) plot showing c_{sf} of A1-LCD variants obtained after 14 days of incubation of samples of 10 μM concentration at 20°C. Individual data points from replicate experiments are shown along with mean ± SEM. **(E)** Negative-stain TEM images showing fibrils formed by A1-LCD variants in the pellets obtained after ultracentrifugation in the assay in (D, right). **(F)** Plot depicting the relative stabilization of fibrils relative to condensates in equilibrium, i.e., $\Delta\Delta G_{gap}$ for all A1-LCD variants. Individual measurements are shown along with the mean ± SEM. All experiments were performed in in 40 mM HEPES buffer, pH 7.0 and 150 mM NaCl.

Next, we measured the stabilities of fibrils by measuring c_{sf}, the saturation concentration for fibril formation. Operationally, we define c_{sf} as the concentration of soluble protein that is left over after fibrillization is complete (*18, 19, 21, 26*). After 14 days of incubation with shaking, the soluble protein concentration stabilized in the low micromolar range independent of the input concentration (**Fig. 1D**, **Fig. S1D**), and we observed fibrils in the pellet by TEM (**Fig. 1E**) and thioflavin T (ThT) fluorescence microscopy (**Fig. S1E**). The c_{sf} values were considerably lower than the corresponding c_{sc} values showing that fibrils are globally stable thermodynamic ground states, whereas condensates are metastable. The pathogenic mutants had lower c_{sf} values than the WT A1-LCD, implying that they form more stable fibrils. This is attributable to the substitution of D262 with V or N, which generates a zipper motif (*27*) that enhances the stability of fibrils (*10, 28*). The c_{sf} values for the variants −4D+4V and −4D+4N were similarly low, showing that the effect of additional aspartate substitutions on fibril stability is minimal. The −3G1S+4V variant also had a c_{sf} value that is equivalent to that of WT A1-LCD.

Our results show that pathogenic mutations within A1-LCD stabilize fibrils and destabilize condensates. This suggests that fibrils and condensates, which are distinct ordered and disordered phases, respectively, are influenced differently by the pathogenic mutations. Additional mutations that we generated, including −4D+4V and −4D+4N are akin to pathogenic mutations in terms of their differential impacts on c_{sf} and c_{sc}, respectively. We quantified the metastability of condensates as $\Delta\Delta G_{gap} = -RT\ln(c_{sf} / c_{sc})$. Here, $R = 1.98\times10^{-3}$ kcal/mol-K is the ideal gas constant and $T = 293$ K. Increasing the magnitude of the free energy gap ($\Delta\Delta G_{gap}$) weakens the metastability of condensates. The free energy gap between metastable condensates and globally stable fibrils increases for pathogenic mutants relative to those of the WT A1-LCD (**Fig. 1F**), showing that pathogenic mutations weaken the metastability of condensates.

How do metastable condensates contribute to fibril formation? The answer comes from Ostwald's rule of stages (*29*): Kinetically accessible states are those that are closest in free energy to the starting state, and this need not be the globally stable phase. We therefore expect metastable condensates to form more readily than fibrils under conditions where the total protein concentration is higher than c_{sc} meaning that the dispersed phase is supersaturated with respect to both fibrils and condensates. Under these conditions, we observe that condensates form more readily than fibrils (**Fig. 1C**).

Metastable condensates decelerate conversion to globally stable fibrils.

The reduced metastability of condensates formed by pathogenic mutants suggests that the free energy barrier to fibril formation is lowered by the mutations, and this should enable comparatively rapid conversion to fibrils. To test this, we characterized the kinetics of fibril formation using ThT fluorescence (*30*). These measurements were performed across a range of protein concentrations where the dispersed phase is subsaturated ($c_{sf} < c_{total} < c_{sc}$) or supersaturated

($c_{total} > c_{sc}$) with respect to condensates (**Fig. 2A, 2B** and **Fig. S2** for repeats of the experiments). In the regime where the dispersed phase is subsaturated with respect to condensates, increases to protein concentration lead to decreases in the lag times for fibril formation and increases in the overall rate of fibril growth for pathogenic mutants. These observations are in line with expectations from classical nucleation-and-growth models (*31-33*). For concentrations that are above c_{sc}, the dispersed phase is supersaturated with respect to both fibrils and condensates, and we observed further decreases in the lag time for fibril formation and increases in the slope that characterizes the growth of fibrils. We computed the inflection points on the growth curves, referred to as t_{node}, and plotted these against the degree of supersaturation, $S_c = \ln(c_{tot}/c_{sc})$, of the dispersed phase with respect to condensates. This analysis showed some variability in absolute values between repeats of the experiment (see **Fig. S2** for additional information). However, it did not reveal any strong changes at $S_c = 0$, which is where the solution transitions from being subsaturated to being supersaturated with respect to condensates (**Fig. 2C, D**). The kinetics of fibril formation of variants −4D+4V and −4D+4N, which exhibit even weaker condensate metastabilities, had similar characteristics relative to those of the pathogenic mutants (**Fig. S3**).

When compared to the pathogenic mutants, WT A1-LCD fibril formation was characterized by longer lag times and slower growth rates (**Fig. 2E** and **Fig. S2** for repeats), and this agrees with the lower stability of the fibrils. Above c_{sc}, we observed that fibril formation shows biphasic behavior, with an initial, relatively fast growth phase followed by a phase with reduced growth rate. The dampening after initial fast growth only occurred in samples where the dispersed phase is supersaturated with respect to condensates ($c_{total} > c_{sc}$). We also note that t_{node} decreased markedly for $S_c > 0$, suggesting that the presence of condensates accelerates nucleation and initial growth (**Fig. 2F**). We also observed similar biphasic kinetics for the −3G1S+4V variant in samples that were supersaturated with respect to condensates (**Fig. S3**). Our observations suggest that while condensates enhance nucleation, they serve as sinks for soluble protein to dampen fibril growth. This sink potential can be quantified in terms of the sequence-specific values of $\Delta\Delta G_{gap}$.

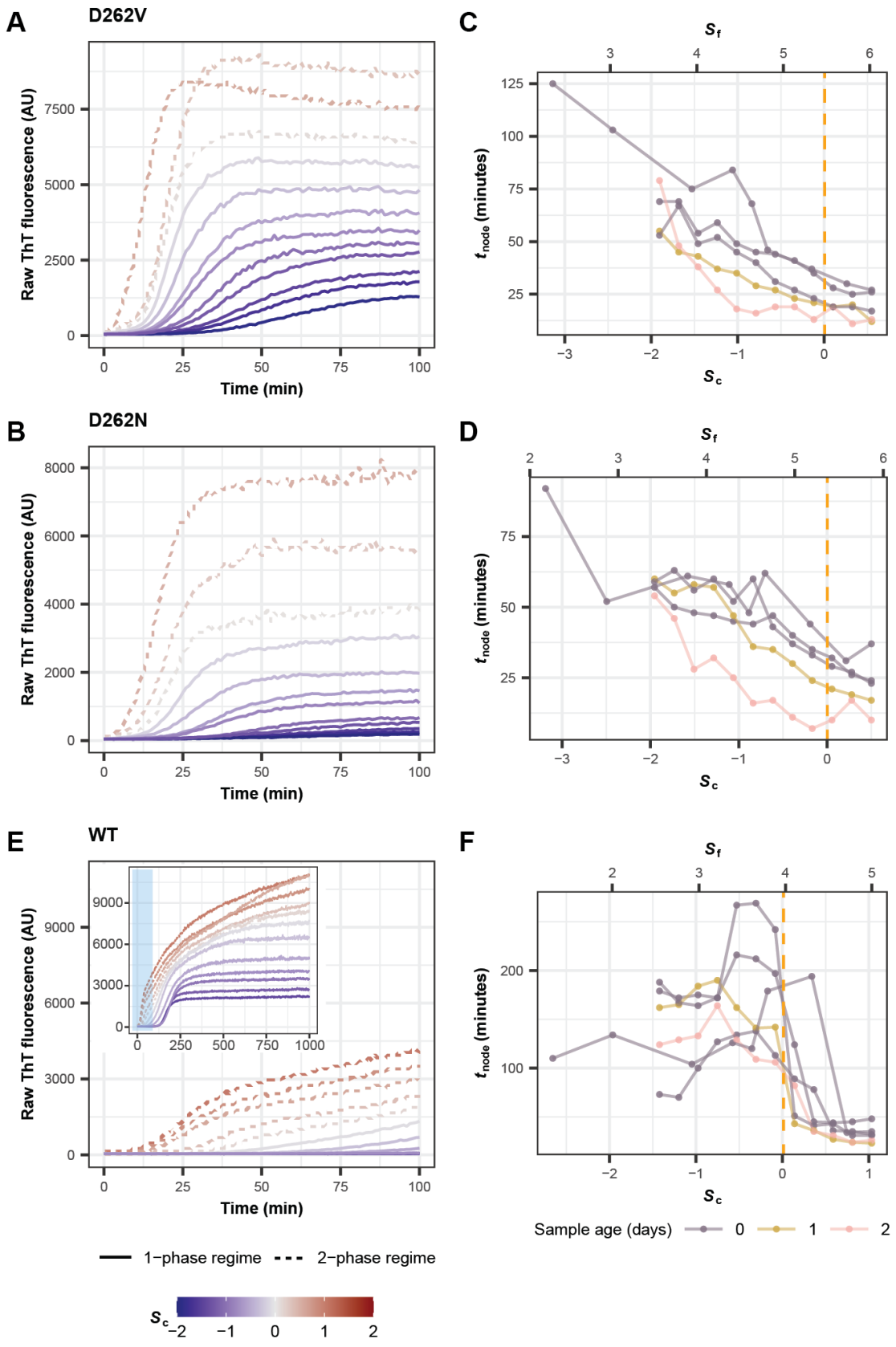

Figure 2: Metastable condensates decelerate conversion to globally stable fibrils.

(A, B, E) Kinetics of fibril formation for A1-LCD variants (A) D262V, (B) D262N and (E) WT monitored by ThT fluorescence across a range of total protein concentrations (c_{total}) that are subsaturated ($S_c < 0$, solid blue lines) or supersaturated ($S_c > 0$ dashed red lines) with respect to condensates. (E) Inset shows the full time course. Data from a single representative experiment is shown; for replicate experiments see **Fig. S2**. **(C, D, F)** Time at which the rate of fibril formation in panels (A, B, E) reaches its maximum (designated as t_{node}) for A1-LCD variants (C) D262V, (D) D262N and (F) WT. The total protein concentrations are quantified as the degree of supersaturation relative to condensate formation (S_c) and fibril formation (S_f). Data from independent experiments are represented by separate line plots. The sample age refers to the age of the sample in native storage buffer without excess salt before initiating condensate formation with addition of NaCl. The dashed vertical line corresponds to $S_c = 0$.

Slow protein efflux from condensates slows fibril formation.

To interpret the kinetics measurements, we analyzed the data using a numerical chemical kinetics approach (*34, 35*). The design of the model (**Fig. 3A**) is based on the following observations: When $S_c > 0$, the overall rate of fibril formation slows down. This is governed by the metastability of condensates, which we characterize using $\Delta\Delta G_{gap}$ that quantifies the sink potential of condensates. The model, which is inspired by the contributions of Knowles and colleagues (*33, 34, 36*), is parsimonious in its design. It includes three phases comprising dilute, dense, and fibrillar phases. Protein exchange between the dilute and dense phase is reversible. The exchange is defined by rate constants for influx and efflux. In accord with the extant literature, fibril formation is defined by rate constants for primary nucleation, elongation, and secondary nucleation (*37, 38*). To minimize the number of fitting parameters, and leveraging observations regarding the global stability of fibrils, we assumed that fibrils are irreversible on the timescale of the simulations. When $S_c < 0$, condensates are absent; accordingly, the influx and efflux rates into and out of condensates are set to zero.

We used the model to fit experimental data for pathogenic mutants and WT for $S_c < 0$ and $S_c > 0$ (**Fig. 3B**). The quality of the fits suggests that the parsimonious model, whereby fibril formation is modeled as occurring predominantly from the dilute phase, is compatible with the data. From the fits, we infer that fibril formation of the WT is slower than that of pathogenic mutants because of slower primary nucleation (**Fig. 3C-3E**). For $S_c > 0$, the rates of primary and secondary nucleation increase for the WT beyond that of the mutants while the rates for the mutants stay relatively unchanged. Furthermore, the ratio of efflux to influx was notably lower for the WT relative to the pathogenic mutants (**Fig. 3F**). In plots that follow the protein fraction in all three phases over time, we observed a rapid decay of the fraction of protein in the dilute and dense phases for the pathogenic mutants, corresponding with rapid fibrillar growth (**Fig. S4**). In contrast, the protein fraction in the dense phase decays more slowly for WT, leading to slower fibrillar growth (**Fig. S4**). Taken together, the data and the model suggest that mutations weaken the sink potential of condensates, thereby tilting the balance in favor of fibrils.

To further explore predictions from the chemical kinetics model, we performed a parameter sweep to test how rate constants for influx and efflux influence the time it takes for 5%, 50% or 95% of the protein to convert to fibrils (**Fig. 3G-I**). All other rate constants were kept constant. A large range of ratios of $k_{dil \rightarrow den}/k_{den \rightarrow dil}$, results in effective incorporation of 5% of the protein ($t_{0.05}$) into fibrils. However, above a certain ratio of $k_{dil \rightarrow den}/k_{den \rightarrow dil}$, $t_{0.05}$ rises sharply and fibril formation is suppressed, indicating that proteins are sequestered in the dense phase when influx into condensates is much faster than efflux. Similarly, the time taken to incorporate 50% of protein into fibrils ($t_{0.5}$) is strongly influenced by the ratio of $k_{dil \rightarrow den}/k_{den \rightarrow dil}$. In this case, we also observed an influence of the absolute value of $k_{den \rightarrow dil}$, whereby below cutoff values of $k_{den \rightarrow dil}$, 50% incorporation into fibrils cannot be reached within 500 minutes. This cutoff value will depend on

the rates for nucleation and growth. The time to reach 95% incorporation into fibrils ($t_{0.95}$) depends even more strongly on $k_{den \rightarrow dil}$ in addition to the ratio of $k_{dil \rightarrow den}/k_{den \rightarrow dil}$. Overall, the analysis shows that the exchange of material between the dilute phase and condensates, particularly the efflux from condensates, can become limiting for fibril growth in the dilute phase. This is highlighted by the WT-like ratio of $k_{dil \rightarrow den}/k_{den \rightarrow dil}$ (**Fig. 3I**, black square) corresponding to a much longer time to reach 95% incorporation into fibrils compared to the pathogenic mutant-like ratio of $k_{dil \rightarrow den}/k_{den \rightarrow dil}$ (**Fig. 3I**, green square).

To test whether condensates can indeed be sinks for soluble protein, we asked if the presence of condensates slowed equilibration to the globally stable fibrillar state. We repeated measurements of the soluble protein concentration after two weeks of incubation with shaking, and the total protein concentrations exceeding c_{sc}. (**Fig. 3J**). Unlike the measurements under conditions where the dispersed phase is subsaturated with respect to condensates ($c_{total} < c_{sc}$), input concentrations above c_{sc} resulted in soluble protein concentrations above c_{sf} even after two weeks of incubation; the higher the input concentrations, i.e., the larger the volume occupied by dense phases, the more soluble protein remained. These results support the interpretation that the presence of condensates slows the achievement of thermodynamic equilibrium because they act as sinks for soluble protein, with their sink potential increasing as $\Delta\Delta G_{gap}$ approaches zero.

According to classical nucleation theories, the rate of nucleation increases and the barrier to nucleation decreases as the dispersed phase becomes increasingly supersaturated with respect to fibrils (*39*). This implies that the rate of fibril growth should increase and the lag time for fibril formation should decrease as the total protein concentration increases. However, for $c_{total} > c_{sc}$, condensates can form and the protein concentrations in the coexisting dilute, and dense phases are fixed. Only the fraction of molecules distributed across the phases and hence the volume occupied by the condensates will change, and yet we observed increased rates of initial fibril formation when $c_{total} > c_{sc}$ and the solutions become increasingly supersaturated with respect to c_{sc}.

Given that increased nucleation cannot be explained by increased concentration, this raises the question of how condensates may contribute to enhanced nucleation. Recent computational analysis showed that the conformations in the outer regions of condensate interfaces formed by PLCDs, including A1-LCD, can form expanded and β-strand-like conformations (*24, 40*). These conformations are likely to be candidates for potentiating interactions that nucleate cross-β structures, akin to preferential adoption of the so-called N* state that is thought to potentiate fibril formation (*41*). Recent experiments have shown that condensate interfaces do indeed accelerate and enable fibril formation (*42*). It has also been shown that condensate interfaces of other systems influence the kinetics of amyloid fibril formation (*43-48*). We used fluorescence microscopy with ThT as a marker to assess whether nucleation and initial growth can originate at the interface of condensates. Low ThT fluorescence throughout the condensates was observed for the WT and −3G1S+4V variant at initial time points, in agreement with the expected small enhancement of fluorescence of molecular rotors by the high viscosity of the condensate interior (*49*) (**Fig. S5**). Over time, ThT fluorescence strongly increased at interfaces of condensates (**Fig. S5A, B**), suggesting that these regions promote fibril nucleation and initial growth. This effect is a likely explanation for the observed decrease in lag time and increase in the rate of fibril formation with increasing fractions of the system volume being taken up by condensates. Recent work showed that aging condensates of full-length FUS proteins comprise different cores and shells (*48*), potentially suggesting a similar mechanism of nucleation at the interface and preservation of soluble protein in the interior.

Taken together, fibril formation can be nucleated by condensate interfaces. However, the interiors of condensates appear to function as sinks, and as a result fibrils grow in the dilute phase. Condensates shrink over time, and the rate of shrinkage is determined by their metastability, with weakly metastable condensates shrinking more rapidly. These inferences are supported by time-lapse microscopy of solutions of A1-LCD that are supersaturated with respect to c_{sc}. (**Movies S1-S3**). We observe that the pathogenic mutants form fibrils that grow rapidly in a small number of places, with concomitant dissolution of condensates (**Movies S1, S2**). WT fibrils, in contrast, form at many condensate interfaces and grow slowly, without individual fibrils dominating fibril growth. WT condensates shrink slowly, limiting WT fibril growth (**Movie S3**).

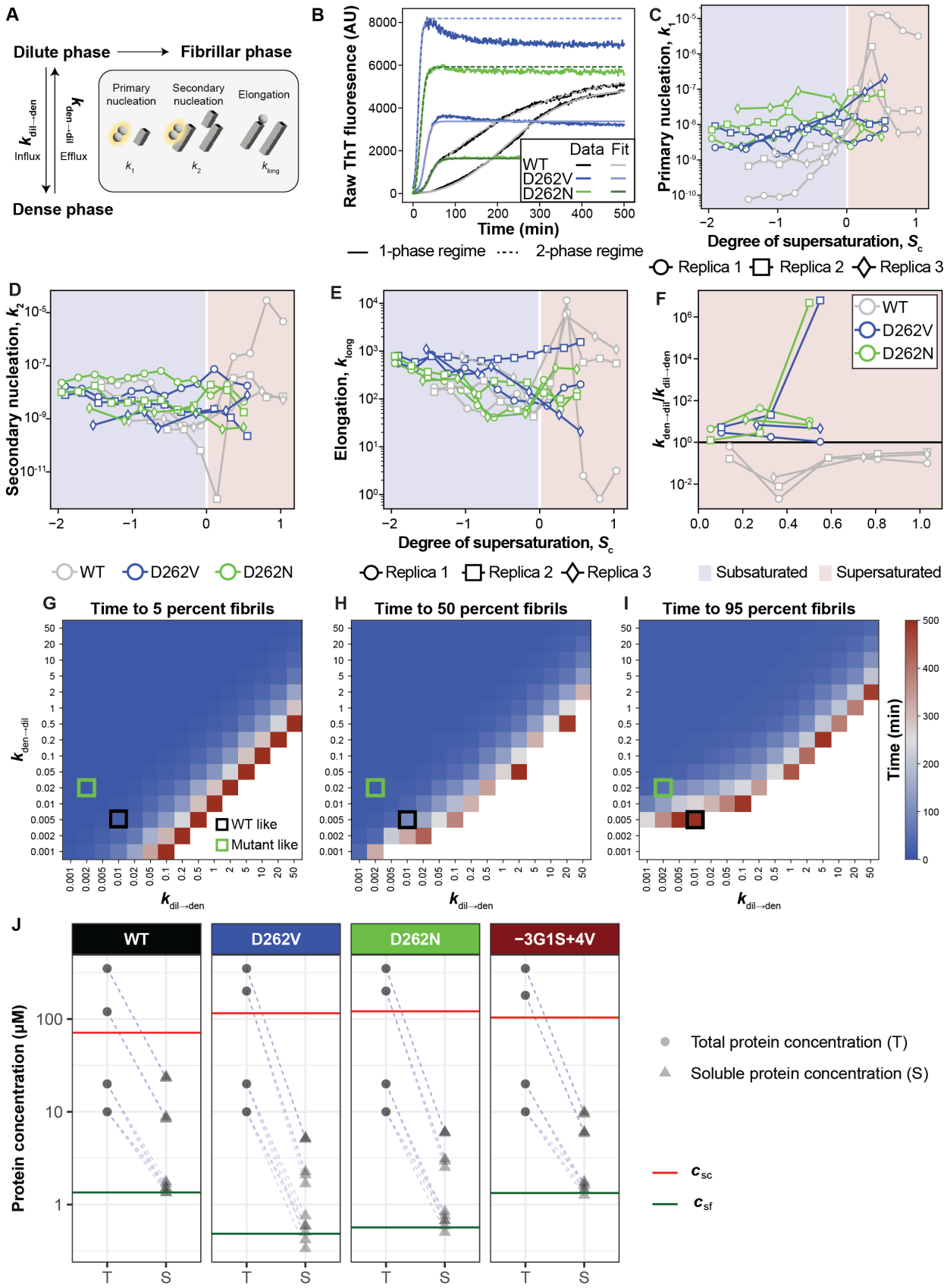

Figure 3: Slow protein efflux from condensates slows fibril formation.

(A) Schematic of the chemical kinetics model used to fit ThT fluorescence curves (see Methods). **(B)** Examples of fits to ThT fluorescence traces for WT (c_{total} = 41 μM, S_c = –0.53), D262V (c_{total} = 65 μM, S_c = –0.57), and D262N (c_{total} = 65 μM, S_c = –0.61) in the 1-phase regime (solid fit lines), and for WT (c_{total} = 128 μM, S_c = +0.59), D262V (c_{total} = 200 μM, S_c = +0.55), and D262N (c_{total} = 200 μM, S_c = +0.50) in the 2-phase regime (dashed fit lines). Concentrations were chosen to ensure similar degrees of subsaturation and supersaturation with respect to c_{sc} for each of the three constructs. **(C-F)** Parameters extracted from fitting ThT fluorescence traces to the chemical kinetics model for all reactions at total concentrations ≥ 17 μM and three replicas performed at sample ages of 0 days. **(G-I)** The effect of titrating $k_{dil\rightarrow den}$ and $k_{den\rightarrow dil}$ on the time to reach **(G)** 5, **(H)** 50, and **(I)** 95 percent fibrils. Here, all other parameters are set to be constant with k_1 = 1e-8, k_2 = 5e-9, k_{long} = 500 and inspired by values extracted from the fits, and the total protein concentration, c_{total} = 200 μM. The total simulation time was 500 minutes. Thus, white values indicate that the target for percent of monomers incorporated into fibrils was not reached within this time. **(J)** Before-and-after plot comparing the input protein concentration and the concentration of soluble protein left in the supernatant after 14 days of incubation, when using different input concentrations above and below c_{sc}. Data from individual measurements are shown. Red lines denote the c_{sc} values for each variant. When fibril formation is initiated under conditions that are sub-saturated with respect to the condensation boundary ($c_{sf} < c_{total} < c_{sc}$), the concentration in the supernatant consistently reaches the same value, which we interpret as c_{sf}. (Data reproduced from **Fig. 1D**, **Fig. S1D**.) However, under conditions that are supersaturated with respect to the condensation boundary ($c_{total} > c_{sc}$), the amount of protein remaining in the supernatant increases, depending on the extent of supersaturation, pointing to the residual sequestration of soluble proteins in condensates even after 14 days of incubation and ultracentrifugation.

Enhancing the metastability of pathogenic mutant condensates suppresses fibril formation.

Condensates can be stabilized by introducing stronger stickers into A1-LCD (*23*). We recently showed that replacing Phe and Tyr with Trp residues enhances the driving force for condensate formation (*50*), and this is also in agreement with the ranking of interaction strengths in other coarse-grained potentials for disordered proteins (*51, 52*). Therefore, we asked if the pathogenic phenotype might be rescued by enhancing condensate metastability through mutagenesis. For this, we designed variants in which we mutated all phenylalanine and tyrosine residues to tryptophan while keeping the sequence around the site of the disease mutation intact (**Fig. 4A**, resulting in allW, allW D262V, or allW D262N). These variants readily formed condensates (**Fig. 4B**), and their c_{sc} values were markedly lower than those of their parental variants (**Fig. 4C**). However, the c_{sf} value for allW was equivalent to that of WT, and those for allW D262V and allW D262N were between those of the original pathogenic mutants and the WT (**Fig. 4D**). All three allW variants formed fibrils within 14 days as confirmed by TEM (**Fig. 4E**). The $\Delta\Delta G_{gap}$ values for the new variants were smaller than those of WT and the original pathogenic mutants (**Fig. 4F**), implying increased metastability of condensates when Phe and Tyr stickers were replaced with Trp.

Although we observed the formation of fibrils for each of the allW variants after prolonged incubation (**Fig. 4E**), ThT assays confirmed a strong kinetic suppression of fibril formation for the allW constructs (**Fig. 4G**, **Fig. S6A, B**). To test whether inhibition also worked in *trans*, we added increasing concentrations of the allW D262N/V variant to a constant concentration of pathogenic mutant protein D262N/V; the resulting condensates concentrated both proteins (**Fig. S6C, D**). Fibril formation was delayed and reduced overall, and this happened in a concentration-dependent manner for pathogenic mutants (**Fig. 4H**). These data support the conclusion that condensates with higher metastability act as sinks for soluble proteins.

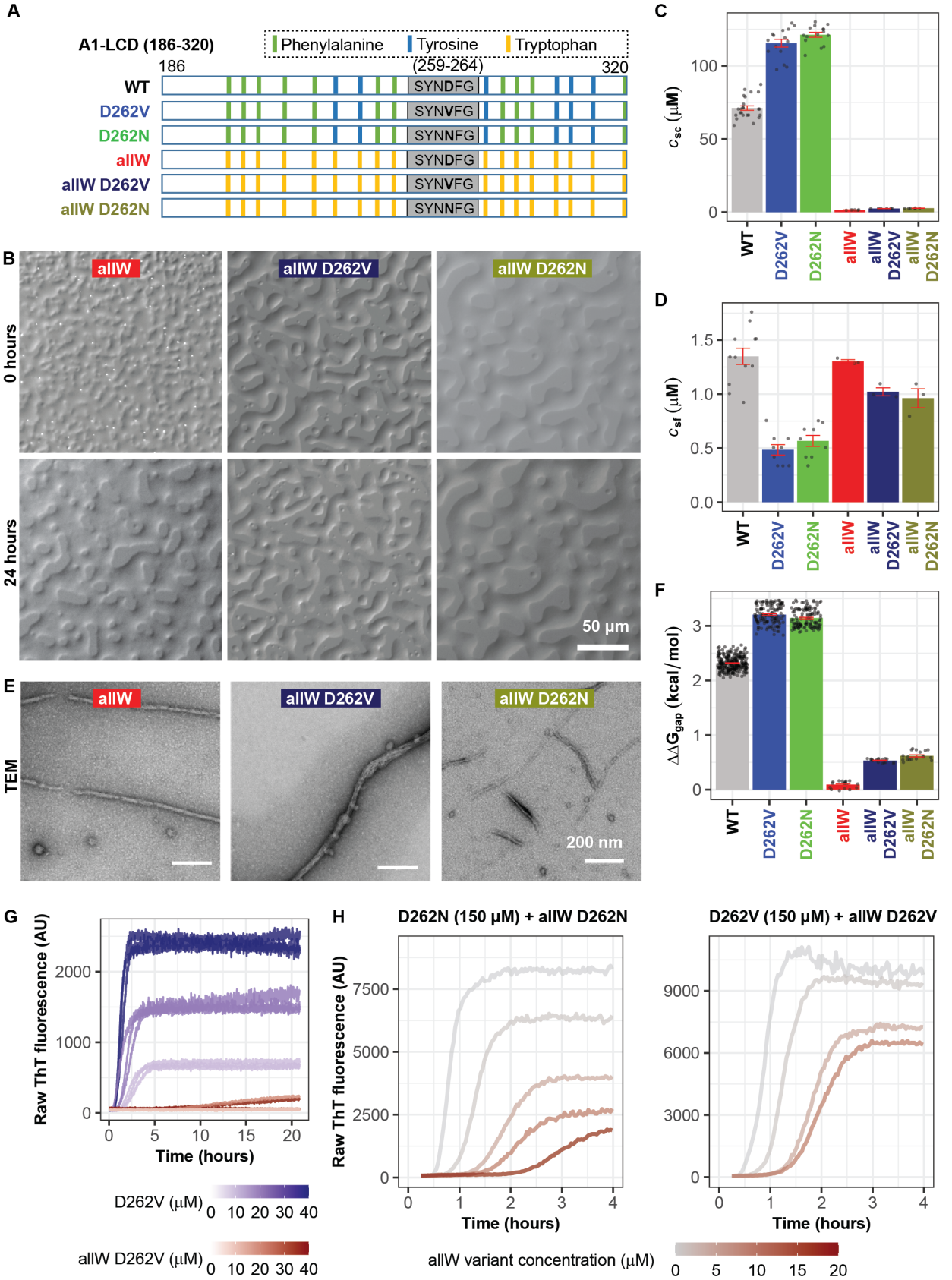

Figure 4: Enhancing the metastability of pathogenic mutant condensates suppresses fibril formation.

(A) Schematic of sequence architectures of A1-LCD wild-type, pathogenic mutants, and the allW variants depicting the sites of mutations. Vertical bars indicate the position of Phe (green), Tyr (blue) or Trp (yellow) residues in the sequence. The motif surrounding the pathogenic mutation site (S_{259}YNDFG_{264}) is shown as a grey rectangle. **(B)** DIC microscopy images of condensates formed by the allW, allW D262V, and allW D262N mutants at 0 hr and 24 hr of incubation. They wet the slide surface. **(C)** Measured c_{sc} values for WT A1-LCD, pathogenic mutants and allW variants. **(D)** Measured c_{sf} values for these variants at 20°C. Individual measurements are shown along with mean ± SEM. Values for WT A1-LCD, D262V and D262N are taken from Fig. 1D. **(E)** Negative-stain TEM images showing fibrils (and some oligomers) formed by allW variants in the pellets obtained after ultracentrifugation in the assay in panel (C). **(F)** $\Delta\Delta G_{gap}$ values for A1-LCD variants. Individual data points calculated from replicate experiments in (C, D) are shown along with the mean ± SEM. **(G)** ThT fluorescence-monitored fibrillization kinetics of A1-LCD variants allW D262V and D262V at equal concentrations showing raw ThT fluorescence as a function of time. Data for the two sequences are shown using red curves (allW D262V) and blue curves (D262V). The color bars show the concentrations for the two sequences. **(H)** Suppression of fibril formation of disease mutants (D262V and D262N) in the presence of increasing concentration of the respective allW variants (allW D262V and allW D262N) depicted through plots of raw ThT fluorescence versus time. All experiments were carried out in in 40 mM HEPES buffer, pH 7.0 and 150 mM NaCl.

Mutations that increase the metastability of A1-LCD condensates rescue a SG disassembly disease phenotype in cells.

Next, we asked if the findings uncovered in the simple system *in vitro* are predictive of properties of SGs in cells. Specifically, we asked if mutations that increase the metastability of condensates formed by homotypic interactions *in vitro* could also rescue a SG-related disease phenotype. SGs are made up of a core network of proteins and RNA, and hnRNPA1 is a relatively minor component (*1*). However, the expression of pathogenic hnRNPA1 mutants slows down SG disassembly dynamics (*53*), and this is reminiscent of the effect of pathogenic mutants of the more abundant component TIA1 (*11*). A typical interpretation of these observations is that fibril formation through homotypic associations of mutant PLCDs disrupts condensate-specific interactions, potentially promoting further homotypic associations to cause a loss of heterotypic buffering (*54*) that leads to slow dynamics and delayed disassembly via energy-dependent processes. Delayed SG disassembly is a pathogenic mutant phenotype in cultured cells (*11, 55*), and we asked if this might be rescued by stabilizing PLCD-mediated condensate formation of hnRNPA1. We replaced aromatic residues in the PLCD of a full-length hnRNPA1 construct with Trp while leaving the zipper motif unchanged as was done in the *in vitro* experiments. U2OS cells expressing the SG marker G3BP1-tdTomato from its endogenous locus were transiently transfected with an eGFP-allW D262V construct. The cells were subjected to heat stress for 1 hour at 43°C, which resulted in the assembly of SGs positive for allW D262V (**Fig. S7A**). Recovery for 2 hours at 37°C resulted in the disassembly of SGs in most cells (**Fig. S7A**).

Next, we transfected cells with constructs that mediate the proportional expression of untagged WT hnRNPA1 or hnRNPA1 variants and eGFP with the help of an internal ribosome entry site (**Fig. 5A**). The cells were subjected to heat stress for 1 hour at 43°C, which resulted in the assembly of SGs positive for the marker PABP and hnRNPA1 (**Fig. S7B**). To test whether increasing the metastability of the pathogenic hnRNPA1 mutant changed the time course of SG disassembly, we transiently expressed the hnRNPA1 variants (from the constructs with the IRES site) in U2OS cells expressing the SG hub G3BP1-dTomato from its endogenous locus (*1*) to enable tracking of SGs in live cells. After one day, the cells were subjected to heat stress at 43°C for 1 hour, triggering SG assembly. Upon release of the stress, achieved by restoring the temperature to 37°C, the SGs disassembled over time, and the rate of disassembly was quantified for cells with moderate expression of eGFP (**Fig. 5B**).

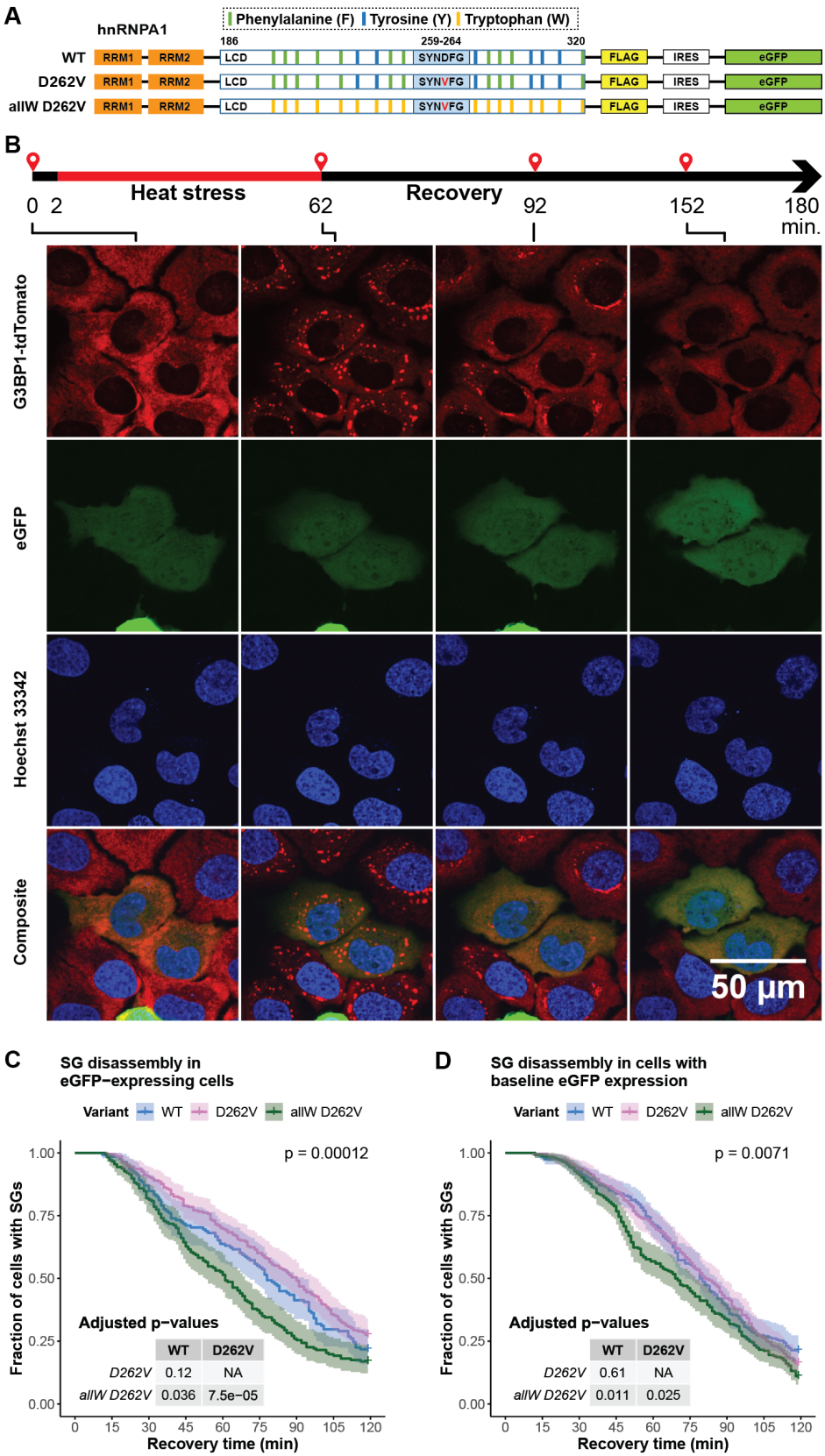

Figure 5: Mutations that increase the metastability of A1-LCD condensates rescue a SG disassembly disease phenotype in cells.

(A) Schematic of the architecture of full-length hnRNPA1 variants with C-terminal FLAG tag and proportionately expressing eGFP via an interim IRES sequence, showing the location and identity of the aromatic residues in the LCD. **(B)** Representative micrographs of U2OS cells expressing the SG marker G3BP1-tdTomato (red) from its endogenous locus, that were transiently transfected with the WT hnRNPA1-FLAG-IRES-eGFP construct and subjected to 1 hour of heat stress at 43 ºC, during which SGs become visible as punctate G3BP1 foci in the cytoplasm. In the recovery phase at 37 °C, the SGs dissolve over time. eGFP (green) identifies the cells expressing protein from the transfected construct. The cell nuclei are stained with Hoechst 33342 (blue). **(C)** Quantification of SG disassembly kinetics in cells expressing eGFP. The mean of three independent replicate experiments is shown. **(D)** Quantification of SG disassembly kinetics from the same experiments as in (C) but of cells without eGFP signal. (C,D) The mean of three independent replicate experiments is shown. The error bars represent the S.E.M. The three variants were compared using a logrank test, and the overall p-value that test for differences between variants is shown in the top right corner. For pairwise comparisons of variants, adjusted p-values (using the Benjamini-Hochberg correction) are shown in the table inset.

Cells expressing the pathogenic hnRNPA1 mutant D262V showed delayed SG disassembly compared to cells expressing hnRNPA1 WT (**Fig. 5C**). The size of the effect of the mutation was comparable to previous observations (*53*). In contrast, in cells expressing the designed mutant protein hnRNPA1 allW D262V, the SGs started to disassemble on timescales that were akin to those of cells expressing the WT protein and completed disassembly even faster than WT. We also analyzed SG disassembly in a population of cells that expressed zero to very low levels of hnRNPA1 variants as indicated by eGFP levels at background levels as a control. SG disassembly dynamics in these cells were identical within error for WT and D262V variants; transfection with the allW D262W variant seemed to confer a slight advantage (**Fig. 5D**). We thus systematically compared SG disassembly dynamics for cells expressing and not expressing each of the constructs, as inferred from the presence or absence of eGFP fluorescence. While the expression of D262V delayed SG disassembly compared to cells that were transfected with the same construct but did not show measurable expression, the expression of WT and allW D262V variants conferred a disassembly enhancement (**Fig. S8**). These experiments suggest that even very low expression levels of hnRNPA1 variants influenced SG disassembly dynamics. Our results suggest that pathogenic mutants of hnRNPA1 with decreased metastability slow SG disassembly. Strikingly, this effect can be rescued by mutations that increase the metastability of condensates, leading to a wild type-like SG disassembly phenotype in cultured cells.

Discussion

Overall, our findings may be summarized as follows: Condensates are metastable relative to globally stable fibrils (**Fig. 1F**). In line with expectations from Ostwald's rule of stages (*29*), condensates form more readily than fibrils (**Fig. 1B**), on sub-second timescales for A1-LCD (*56*), but the system converts to the globally stable fibrillar state (**Figs. 1B, 2, 3J**). The metastability of condensates relative to fibrils is an important factor in determining the timescale of conversion to fibrils. Conversion can be slow if condensates have increased metastability defined by lower values of $\Delta\Delta G_{gap}$ because condensates can serve as effective sinks for soluble proteins (**Fig. 3J**). The pathogenic mutations in the A1-LCD weaken the metastability of condensates to stabilize fibrils (**Figs. 1D, 1F**). Condensates formed by pathogenic mutants do not sequester soluble protein as readily as WT condensates (**Figs. 2, 3**). Interfaces of condensates can nucleate fibril formation (**Fig. 2, Fig. S5**). However, fibril growth occurs in the dilute phase and elongation is determined by the protein concentration available in the dilute phase and hence the efflux (**Fig. 3**). Our experiments in cells show that introducing mutations that weaken the metastability of A1-LCD condensates also has a deleterious effect on SG disassembly. Conversely, mutations that increase

the metastability of the condensates formed by pathogenic mutants *in vitro* also rescue the SG disassembly phenotype in cells (**Fig. 5C**).

Surprisingly, increasing the metastability of condensates formed by PLCDs suppresses fibril formation, and in the cellular context this facilitates SG disassembly even when disease-associated mutations are present. Kinetic stabilization against fibrillization has also recently been proposed for translation-repressing condensates formed by CPEB4 (*57*). Our findings point to separable contributions of stickers that contribute to stabilization of disordered condensates and zippers that stabilize ordered, fibrillar phases (*53*). These separable interactions likely contribute to sticker-mediated heterotypic buffering through interactions among networks of PLCDs within SGs (*40, 54*). Recent work has suggested that the formation of separate TDP-43 condensates, either via oxidative stress, protein unfolding stress, or optogenetic engineering, and therefore loss of heterotypic buffering, promotes conversion to solid states and pathogenetic processes (*15, 58*), highlighting the importance of networks of complementary interactions among PLCDs.

Our results suggest that disease-associated mutations in A1-LCD are separation-of-function mutations that destabilize condensates and stabilize fibrils. Conversely, the introduction of Trp residues strongly stabilizes condensates but has little influence on fibril stability. Previous experiments removed protein sections containing stickers and fibril-forming motifs concurrently and therefore had directionally similar effects on the driving force for condensation and fibril formation (*28, 59-62*). This led to the questionable conclusion that fibrils and condensates formed via the same interactions. Instead, we conclude, based on our data, that the molecular grammars underlying condensate and fibril formation are overlapping in sequence but separable because of differences in sticker- versus zipper-mediated interactions.

Based on our findings, we propose that SGs are unlikely to be crucibles of amyloid formation. Instead, they are likely to be protective against fibril formation through networks of sticker-mediated homotypic and heterotypic interactions of PLCDs (*54*). However, given the metastable nature of condensates, prolonged stress or the presence of destabilizing pathogenic mutations may render this buffering function less effective, and as a result, homotypic interactions among PLCDs might drive the formation of solid inclusions.

Acknowledgments: Microscopy images were acquired at the Cell and Tissue Imaging Center at SJCRH, which is supported by SJCRH and NCI (grant P30 CA021765). We thank Hong Joo Kim and Brian Freibaum from the Taylor lab, Richard Kriwacki, and Kresten Lindorff-Larsen for insightful discussions.

Funding: This research was supported by NIH grants R01NS121114 (to R.V.P. and T.M.), and grant R35NS097974 (to J.P.T.), the St. Jude Research Collaborative on the Biology and Biophysics of RNP granules (to J.P.T., R.V.P., and T.M.), and the American Lebanese Syrian Associated Charities (to J.P.T. and T.M.).

Author contributions: Conceptualization: RVP, TM; Methodology: TD, FZ, MF, KMR, JM, JPT, RVP, TM; Investigation: TD, FZ, MF, KMR; Visualization: TD, FZ, MF, KMR, RVP, TM; Funding acquisition: JPT, RVP, TM; Supervision: RVP, TM; Writing – original draft: TD, FZ, RVP, TM; Writing – review & editing: all authors.

Competing interests: R.V.P. is a member of the Scientific Advisory Board and a shareholder of Dewpoint Therapeutics. The work reported here was not influenced by this affiliation. The remaining authors declare no competing interests.

References

1. P. Yang *et al.*, G3BP1 Is a Tunable Switch that Triggers Phase Separation to Assemble Stress Granules. *Cell* **181**, 325-345 e328 (2020).
2. D. W. Sanders *et al.*, Competing Protein-RNA Interaction Networks Control Multiphase Intracellular Organization. *Cell* **181**, 306-324 e328 (2020).
3. J. Guillen-Boixet *et al.*, RNA-Induced Conformational Switching and Clustering of G3BP Drive Stress Granule Assembly by Condensation. *Cell* **181**, 346-361 e317 (2020).
4. J. Wang *et al.*, A Molecular Grammar Governing the Driving Forces for Phase Separation of Prion-like RNA Binding Proteins. *Cell* **174**, 688-699.e616 (2018).
5. J. P. Taylor, Multisystem proteinopathy. *Intersecting genetics in muscle, bone, and brain degeneration* **85**, 658-660 (2015).
6. P. Ciryam *et al.*, Spinal motor neuron protein supersaturation patterns are associated with inclusion body formation in ALS. *Proceedings of the National Academy of Sciences* **114**, E3935-E3943 (2017).
7. N. E. Farrawell *et al.*, Distinct partitioning of ALS associated TDP-43, FUS and SOD1 mutants into cellular inclusions. *Scientific Reports* **5**, 13416 (2015).
8. M. Neumann *et al.*, FET proteins TAF15 and EWS are selective markers that distinguish FTLD with FUS pathology from amyotrophic lateral sclerosis with FUS mutations. *Brain* **134**, 2595-2609 (2011).
9. E. Kabashi *et al.*, TARDBP mutations in individuals with sporadic and familial amyotrophic lateral sclerosis. *Nature Genetics* **40**, 572-574 (2008).
10. H. J. Kim *et al.*, Mutations in prion-like domains in hnRNPA2B1 and hnRNPA1 cause multisystem proteinopathy and ALS. *Nature* **495**, 467-473 (2013).
11. I. R. Mackenzie *et al.*, TIA1 Mutations in Amyotrophic Lateral Sclerosis and Frontotemporal Dementia Promote Phase Separation and Alter Stress Granule Dynamics. *Neuron* **95**, 808-816 e809 (2017).
12. A. Patel *et al.*, A Liquid-to-Solid Phase Transition of the ALS Protein FUS Accelerated by Disease Mutation. *Cell* **162**, 1066-1077 (2015).
13. T. Nomura *et al.*, Intranuclear aggregation of mutant FUS/TLS as a molecular pathomechanism of amyotrophic lateral sclerosis. *Journal of Biological Chemistry* **289**, 1192-1202 (2014).
14. Y. R. Li, O. D. King, J. Shorter, A. D. Gitler, Stress granules as crucibles of ALS pathogenesis. *Journal of Cell Biology* **201**, 361-372 (2013).
15. S. Lu *et al.*, Heat-shock chaperone HSPB1 regulates cytoplasmic TDP-43 phase separation and liquid-to-gel transition. *Nature Cell Biology* **24**, 1378-1393 (2022).
16. A. Molliex *et al.*, Phase separation by low complexity domains promotes stress granule assembly and drives pathological fibrillization. *Cell* **163**, 123-133 (2015).
17. T. C. T. Michaels *et al.*, Amyloid formation as a protein phase transition. *Nature Reviews Physics* **5**, 379-397 (2023).
18. S. L. Crick, K. M. Ruff, K. Garai, C. Frieden, R. V. Pappu, Unmasking the roles of N- and C-terminal flanking sequences from exon 1 of huntingtin as modulators of polyglutamine aggregation. *Proceedings of the National Academy of Sciences* **110**, 20075-20080 (2013).
19. A. E. Posey *et al.*, Profilin reduces aggregation and phase separation of huntingtin N-terminal fragments by preferentially binding to soluble monomers and oligomers. *Journal of Biological Chemistry* **293**, 3734-3746 (2018).

20. K. M. Ruff *et al.*, Sequence grammar underlying the unfolding and phase separation of globular proteins. *Mol Cell* **82**, 3193-3208 e3198 (2022).
21. K. Garai, B. Sahoo, P. Sengupta, S. Maiti, Quasihomogeneous nucleation of amyloid beta yields numerical bounds for the critical radius, the surface tension, and the free energy barrier for nucleus formation. *The Journal of Chemical Physics* **128**, (2008).
22. E. W. Martin *et al.*, Valence and patterning of aromatic residues determine the phase behavior of prion-like domains. *Science* **367**, 694-699 (2020).
23. A. Bremer *et al.*, Deciphering how naturally occurring sequence features impact the phase behaviours of disordered prion-like domains. *Nature Chemistry* **14**, 196-207 (2022).
24. M. Farag *et al.*, Condensates formed by prion-like low-complexity domains have small-world network structures and interfaces defined by expanded conformations. *Nature Communications* **13**, 7722 (2022).
25. R. V. Pappu, S. R. Cohen, F. Dar, M. Farag, M. Kar, Phase Transitions of Associative Biomacromolecules. *Chemical Reviews* **123**, 8945-8987 (2023).
26. A. K. Buell, C. M. Dobson, T. P. J. Knowles, The physical chemistry of the amyloid phenomenon: thermodynamics and kinetics of filamentous protein aggregation. *Essays in Biochemistry* **56**, 11-39 (2014).
27. D. Eisenberg, M. Jucker, The amyloid state of proteins in human diseases. *Cell* **148**, 1188-1203 (2012).
28. X. Gui *et al.*, Structural basis for reversible amyloids of hnRNPA1 elucidates their role in stress granule assembly. *Nature Communications* **10**, 2006 (2019).
29. W. Ostwald, Studien uber die Bildung und Umwandlung fester Körper. *Zeitschrift für Physikalische Chemie* **22**, 289-330 (1897).
30. H. Naiki, K. Higuchi, M. Hosokawa, T. Takeda, Fluorometric determination of amyloid fibrils in vitro using the fluorescent dye, thioflavin T1. *Analytical Biochemistry* **177**, 244-249 (1989).
31. F. Ferrone, Analysis of protein aggregation kinetics. *Methods Enzymol* **309**, 256-274 (1999).
32. W. F. Xue, S. W. Homans, S. E. Radford, Systematic analysis of nucleation-dependent polymerization reveals new insights into the mechanism of amyloid self-assembly. *Proceedings of the National Academy of Sciences* **105**, 8926-8931 (2008).
33. P. Arosio, T. P. Knowles, S. Linse, On the lag phase in amyloid fibril formation. *Phys Chem Chem Phys* **17**, 7606-7618 (2015).
34. T. P. J. Knowles *et al.*, An Analytical Solution to the Kinetics of Breakable Filament Assembly. *Science* **326**, 1533-1537 (2009).
35. G. Meisl *et al.*, Molecular mechanisms of protein aggregation from global fitting of kinetic models. *Nature Protocols* **11**, 252-272 (2016).
36. T. P. J. Knowles *et al.*, Kinetics and thermodynamics of amyloid formation from direct measurements of fluctuations in fibril mass. *Proceedings of the National Academy of Sciences* **104**, 10016-10021 (2007).
37. T. C. T. Michaels *et al.*, Chemical Kinetics for Bridging Molecular Mechanisms and Macroscopic Measurements of Amyloid Fibril Formation. *Annual Review of Physical Chemistry* **69**, 273-298 (2018).
38. A. K. Buell *et al.*, Secondary nucleation of monomers on fibril surface dominates α-synuclein aggregation and provides autocatalytic amyloid amplification. *Quarterly Reviews of Biophysics* **50**, e6 (2017).

39. D. W. Oxtoby, Nucleation of First-Order Phase Transitions. *Accounts of Chemical Research* **31**, 91-97 (1998).
40. M. Farag, W. M. Borcherds, A. Bremer, T. Mittag, R. V. Pappu, Phase separation of protein mixtures is driven by the interplay of homotypic and heterotypic interactions. *Nature Communications* **14**, 5527 (2023).
41. M. S. Li, D. K. Klimov, J. E. Straub, D. Thirumalai, Probing the mechanisms of fibril formation using lattice models. *The Journal of Chemical Physics* **129**, (2008).
42. M. Linsenmeier *et al.*, The interface of condensates of the hnRNPA1 low-complexity domain promotes formation of amyloid fibrils. *Nature Chemistry* **15**, 1340-1349 (2023).
43. W. P. Lipiński *et al.*, Biomolecular condensates can both accelerate and suppress aggregation of α-synuclein. *Science Advances* **8**, eabq6495.
44. L. Emmanouilidis *et al.*, A solid beta-sheet structure is formed at the surface of FUS liquid droplets during aging. *bioRxiv* **https://doi.org/10.1101/2023.06.02.542764**, (2023).
45. C. He, C. Y. Wu, W. Li, K. Xu, Multidimensional super-resolution microscopy unveils nanoscale surface aggregates in the aging of FUS condensates. *Journal of the American Chemical Society* **145**, 24240–24248 (2023).
46. D. Pantoja-Uceda *et al.*, Phe-Gly motifs drive fibrillization of TDP-43's prion-like domain condensates. *PLoS Biology* **19**, e3001198 (2021).
47. D. Maltseva *et al.*, Fibril formation and ordering of disordered FUS LC driven by hydrophobic interactions. *Nature Chemistry* **15**, 1146-1154 (2023).
48. Y. Shen *et al.*, The liquid-to-solid transition of FUS is promoted by the condensate surface. *Proceedings of the National Academy of Sciences* **120**, e2301366120 (2023).
49. P. Mukherjee, S. Ganai, Thioflavin-T: A Quantum Yield-Based Molecular Viscometer for Glycerol-Monohydroxy Alcohol Mixtures. *ACS Omega* **8**, 36604-36613 (2023).
50. I. Alshareedah *et al.*, Sequence-specific interactions determine viscoelasticity and aging dynamics of protein condensates. *bioRxiv* **https://doi.org/10.1101/2023.04.06.535902**, (2023).
51. G. Tesei, T. K. Schulze, R. Crehuet, K. Lindorff-Larsen, Accurate model of liquid-liquid phase behavior of intrinsically disordered proteins from optimization of single-chain properties. *Proceedings of the National Academy of Sciences* **118**, (2021).
52. J. A. Joseph *et al.*, Physics-driven coarse-grained model for biomolecular phase separation with near-quantitative accuracy. *Nature Computational Science* **1**, 732-743 (2021).
53. D. Beijer *et al.*, Characterization of HNRNPA1 mutations defines diversity in pathogenic mechanisms and clinical presentation. *Journal of Clinical Investigation Insight* **6**, (2021).
54. C. Mathieu, R. V. Pappu, J. P. Taylor, Beyond aggregation: Pathological phase transitions in neurodegenerative disease. *Science* **370**, 56-60 (2020).
55. D. Beijer *et al.*, Characterization of HNRNPA1 mutations defines diversity in pathogenic mechanisms and clinical presentation. *JCI Insight* **6**, (2021).
56. E. W. Martin *et al.*, A multi-step nucleation process determines the kinetics of prion-like domain phase separation. *Nature Communications* **12**, 4513 (2021).
57. C. Garcia-Cabau *et al.*, Kinetic stabilization of translation-repression condensates by a neuron-specific microexon. *bioRxiv* **https://doi.org/10.1101/2023.03.19.532587**, (2023).
58. C. G. Otte *et al.*, Optogenetic TDP-43 nucleation induces persistent insoluble species and progressive motor dysfunction in vivo. *Neurobiology of Disease* **146**, 105078 (2020).
59. M. Kato *et al.*, Cell-free formation of RNA granules: low complexity sequence domains form dynamic fibers within hydrogels. *Cell* **149**, 753-767 (2012).

60. D. T. Murray *et al.*, Structure of FUS Protein Fibrils and Its Relevance to Self-Assembly and Phase Separation of Low-Complexity Domains. *Cell* **171**, 615-627 e616 (2017).
61. M. P. Hughes *et al.*, Atomic structures of low-complexity protein segments reveal kinked beta sheets that assemble networks. *Science* **359**, 698-701 (2018).
62. F. Luo *et al.*, Atomic structures of FUS LC domain segments reveal bases for reversible amyloid fibril formation. *Nature Structural Molecular Biology* **25**, 341-346 (2018).
63. F. W. Studier, Protein production by auto-induction in high density shaking cultures. *Protein Expr Purif* **41**, 207-234 (2005).
64. N. M. Milkovic, T. Mittag, in *Intrinsically Disordered Proteins: Methods and Protocols,* B. B. Kragelund, K. Skriver, Eds. (Springer US, New York, NY, 2020), pp. 685-702.
65. A. Bremer *et al.*, Deciphering how naturally occurring sequence features impact the phase behaviours of disordered prion-like domains. *Nat Chem* **14**, 196-207 (2022).
66. G. Meisl *et al.*, Molecular mechanisms of protein aggregation from global fitting of kinetic models. *Nat Protoc* **11**, 252-272 (2016).
67. Y. Benjamini, Y. Hochberg, Controlling the False Discovery Rate: A Practical and Powerful Approach to Multiple Testing. *Journal of the Royal Statistical Society: Series B* **57**, 289-300 (1995).